

A Comparative Investigation on the Corrosion Behavior of cast and rolled ZG21 Mg Alloys

Peng Chen, Yingwei Song*, Jinhui Liu, Dayong Shan, En-Hou Han

Key Laboratory of Nuclear Materials and Safety Assessment, Institute of Metal Research, Chinese Academy of Sciences, Shenyang 110016, China

*E-mail: ywsong@imr.ac.cn

Received: 11 January 2017 / Accepted: 24 March 2017 / Published: 12 April 2017

ZG21 Mg alloys exhibit excellent deformation ability at room temperature. However, their corrosion behavior lacks sufficient investigation. The relationship between the second phases and micro-galvanic corrosion of ZG21 Mg alloys has been investigated using Atomic Force Microscopy (AFM), Scanning Kelvin Probe Force Microscopy (SKPFM), and electrochemical measurements. $Mg_3Zn_3Gd_2$ second phases act as micro-cathodes due to their nobler potential than α -Mg matrix. Localized corrosion occurs at cast ZG21, whereas general corrosion occurs at rolled ZG21. The rolled alloy shows better corrosion resistance owing to the relatively more homogeneous distribution and finer second phases.

Keywords: Second phases; ZG21 Mg alloys; AFM; SKPFM; Micro-cathodes

1. INTRODUCTION

Although magnesium alloys exhibit good mechanical properties [1, 2], their relatively inferior corrosion property at current stage is still a serious obstacle to the increasingly widespread applications [3, 4]. As a result, abundant work has been carried out to gain insight into the corrosion mechanism of magnesium alloys [5-9]. As we all know, low standard electrochemical potential of Mg (-2.4 V_{SHE}) is the primary reason for its susceptibility to corrosion. The morphology and structure of the surface film also contribute to the poor corrosion resistance [4, 6, 10]. Especially, the second phases in magnesium alloys have been attracted strong interest due to their great influence on corrosion behavior [11-15]. For example, Song et al. reported that the β -Mg₁₇Al₁₂ phases in AZ91 Mg alloy exhibit a dual purpose in corrosion [5, 16]. It is generally recognized that the β -Mg₁₇Al₁₂ phases act either as micro-galvanic cathodes accelerating the corrosion of α -Mg matrix due to their more positive corrosion potential or as network barrier to hinder corrosion propagation in the matrix. The later is in consistent with the report that β -Mg₁₇Al₁₂ phases can reduce the corrosion rate of AZ91 by forming corrosion resistant barrier

because of the precipitation of Al-rich coring structure along grain boundaries [17]. Most of the previous results are concerned with the micro-galvanic role of second phases in corrosion process, and the second phases mainly act as micro-cathodes because of their nobler potential than matrix [11, 14, 18]. However our recent study, published in another paper [19, 20], shows that the second phases in EW75 act as micro-anodes and exhibit lower electrochemical stability in comparison with Mg matrix. In addition, the size and distribution of second phases in cast Mg alloys will change greatly after forming treatment, possible from micrometer scale with network distribution to nanometer scale with discrete distribution, which will dramatically influence the corrosion behavior of Mg alloys. However, the previous studies [21-23] on the size effect of second phases are mainly based on micrometer scale. It is far from sufficient to disclose the influence of second phases on the corrosion behavior of Mg alloys. Abundant work is very necessary to clarify the corrosion mechanism of Mg alloys influenced by second phases.

In recent years, some new Mg alloys, with addition of zirconium and rare-earth (RE) elements, have been developed to improve mechanical properties for various practical applications [24, 25]. ZG21 (Mg-2Zn-0.8Gd-0.4Zr), a recently developed Mg alloy by Institute of Metal Research, Chinese Academy of Sciences, exhibits excellent forming property at room temperature [26-29]. However, the knowledge related to the corrosion behavior of this alloy is far from enough. Especially, Zn is inerter than Mg, whereas Gd is more active than Mg. The role of the second phases in the micro-galvanic corrosion of ZG21 is not clear. The local electrochemical inhomogeneities can result in a more complicated corrosion mechanism [30-33].

The previous studies [11, 14, 17, 34] on the micro-galvanic roles of second phases are mainly based on the conventional techniques, such as electrochemical methods and morphologies investigation. Fortunately, the scanning probe microscope (SPM), which can be used to measure the surface roughness of Mg substrate as well as the relative Volta potential differences between second phases and matrix, makes it more convenient to investigate the role of second phases in corrosion behavior. Some previous studies [12, 35, 36] prove that Atomic Force Microscopy (AFM) and Scanning Kelvin Probe Force Microscopy (SKPFM) are powerful tools to characterize the second phases and Mg matrix, and further to disclose the electrochemical corrosion process.

Thus, this paper aims to clarify the influence of second phases on the corrosion behavior of ZG21 Mg alloys, especially the micro-galvanic interaction between the second phases and Mg matrix. A sequence of investigations also have been carried out to determine the relationship between the distribution and size of second phases and the corrosion rate of ZG21 Mg alloys.

2. EXPERIMENTAL

2.1 Materials

Experimental materials used in this investigation were the cast and rolled ZG21 alloy plates with chemical composition (wt.%) of 2.26 Zn, 0.74 Gd, 0.41 Zr, and Mg balance. The alloys were produced with high-purity 99.9% Mg, 99.9% Zn, 99.9% Gd, and 99.9% Zr by resistance melting under the

protection of a mixed gas atmosphere of SF₆(1 vol.%) and CO₂(99 vol.%). The chemical composition (wt.%) of the high-purity Mg is 0.01 Si, 0.01 Al, 0.0032 Fe, 0.0012 Cu, 0.01 Mn, and Mg balance. The rolling experiment was conducted through two steps: rough rolling and finish rolling [27, 28].

2.2 Samples

The samples for microstructure investigation, AFM and SKPFM measurements were cut into 10 mm×10 mm×1.0 mm sheets, then mechanically ground with silicon carbide (SiC) papers to 5000 grit and polished using diamond pastes (1 μm).

The samples for immersion, XRD, polarization curves, and EIS tests were successively ground to 3000 grit paper, ultrasonically cleaned in acetone, then dried in cold air.

2.3 Structure characterization

Microstructure and corrosion morphologies were observed using a Phillips XL30 scanning electron microscopy (SEM) equipped with an energy dispersive X-ray spectroscopy (EDX). The phase structure of the ZG21 alloys was measured using a Philips PW1700 X-ray diffraction (XRD) with Cu target ($k = 0.154$ nm). The XRD patterns were analyzed with MDI Jade 5.0 software. The cast and rolled samples were immersed in 3.5% NaCl solution for 30 min, 1 h, 5 h, and 24 h, respectively, and then the surface morphologies after the removal of corrosion products using 180 g L⁻¹ chromic acid solution were observed using SEM.

2.4 AFM and SKPFM experiments

AFM and SKPFM measurements were carried out using MultiMode IID Scanning Probe Microscopy (SPM) System (Bruker Corporation, Santa Barbara, CA). The AFM and SKPFM results were analyzed by NanoScope Analysis software.

All the measurements were conducted at room temperature. The probe used in SKPFM measurements was magnetic etched silicon probe (MESP) ($k=2.8$ N/m, Bruker Corporation, CA, USA) with its tip coated by Co/Cr alloy. Prior to each experiment, the tip was checked by performing a potential measurement on a reference sample. A dual scan mode was used for the SKPFM measurement. The tapping mode was applied in the first scan to obtain surface topography signal, and then the cantilever was lifted up 50 nm in the second scan to record the potential signal of the scanned area.

After AFM and SKPFM measurements, the same specimen was used for SEM observation. Before the SEM tests, the specimens were ultrasonically cleaned in ethanol to remove the remnant corrosion products, and finally dried in air.

2.5 Corrosion tests

Corrosion resistance was studied by weight loss rate, polarization curves, and Electrochemical Impedance Spectroscopy (EIS) tests.

In the case of weight loss rate tests, the samples with size of 80 mm×40 mm×10 mm were immersed in 3.5 % NaCl solution (placed in 2000 ml beakers) for 72 h. Since hydrogen evolution reaction can promote the pH value of NaCl solution, the solution was updated every 12 h to maintain a stable pH value. The weight of the samples before immersion experiments and after the removal of corrosion products was measured using an analytical balance with a precision of 0.1 mg. Corrosion rate (V) was calculated in terms of the following equation:

$$V = \Delta W / St \quad (1)$$

where ΔW is the weight loss of the specimen; S is the total area of the specimen; and t is the immersion time.

Three experimental measurements were carried out for each case, and the final results were the average values of these three measurements.

The electrochemical tests were carried out using PARSTAT4000 electrochemistry test system (Princeton Applied Research, USA). All of the tests were carried out in a corrosion cell containing 3.5% NaCl solution with standard three electrode configuration: saturated calomel as reference electrode, a platinum sheet as counter electrode, and the specimen with an exposure area of 1 cm² as working electrode. An initial delay of 300 s was set to ensure a stable system before the experiments were undertaken. The potentiodynamic curve measurements were started from -200 mV vs. open circuit potential (OCP) at a constant scan rate of 0.5 mV s⁻¹ until a final current density of approximately 10 mA cm⁻². Polarization curves were fitted using the CorrView software in the mode of Tafel (traditional). Electrochemical impedance spectroscopy (EIS) measurements were also carried out using PARSTAT4000 electrochemistry test system (Princeton Applied Research, USA) under open circuit potential (OCP), and it is mandatory to achieve a stable state before each test . The scan frequency ranged from 100 kHz to 0.01 Hz with a perturbation amplitude of 5 mV. The EIS spectra were fitted using the ZSimpWin 3.20 software.

3. RESULTS

3.1 Microstructure and phase composition of ZG21 Mg alloys

Microstructures of the cast and rolled ZG21 alloys are shown in Fig. 1. The cast ZG21 alloy (Fig.1a) exhibits an inhomogeneous microstructure. Abundant white second phases, with network but discrete distribution, are observed on the grain boundaries. The dimensions of these second phases range from several to tens micrometers. Nevertheless, the fine second phases in the rolled ZG21 alloy, with the dimension of only several hundred nanometers, are randomly distributed in the entire surface (Fig. 1b). It is evident that the second phases are more uniformly distributed in the rolled alloy than in the cast alloy.

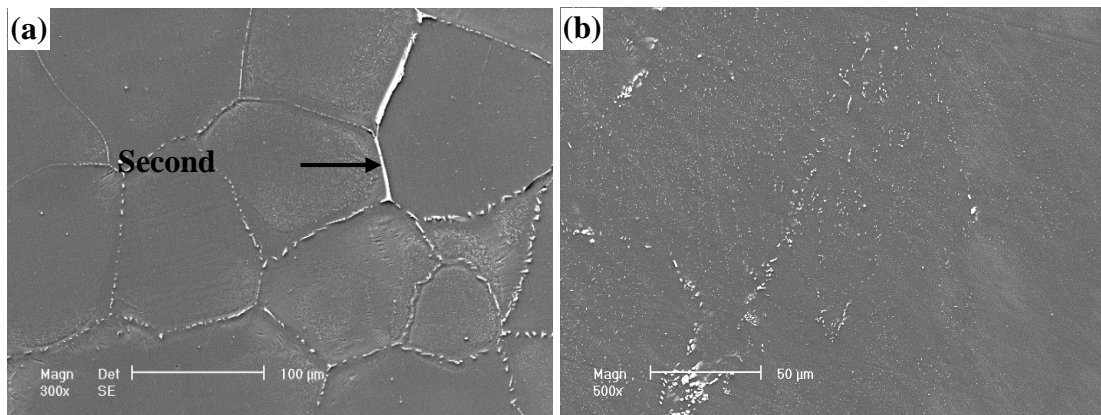


Figure 1. Microstructures of ZG21 Mg alloys: (a) cast, and (b) rolled

The EDX analysis reveals that white second phases in the cast ZG21 alloy are composed of Mg, Zn, and Gd. The atomic ratio of Zn and Gd is near to 3:2, and superfluous Mg can be attributed to the effect of Mg matrix. Furthermore, the phase structure of both alloys is identified by XRD (Fig. 2). The α -Mg matrix and $Mg_3Zn_3Gd_2$ second phases are detected. This result is in good agreement with the EDX analysis. It should be noted that there is no difference in the chemical composition of the second phases between the cast and rolled alloys. Thus, further studies about the micro-galvanic role of the second phases mainly focus on the cast ZG21 alloy because of its large second phases with convenient investigation.

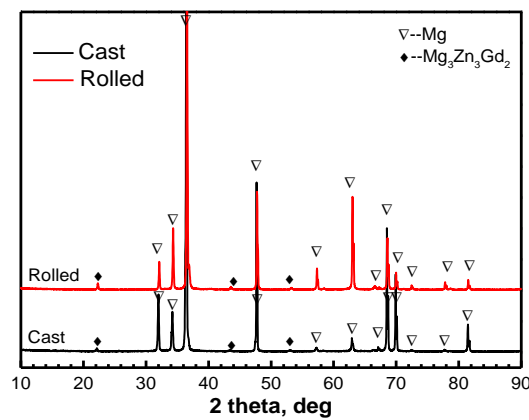


Figure 2. XRD patterns of the cast and rolled ZG21 Mg alloys

3.2 Height and Volta potential distribution of the cast ZG21 alloy

All the AFM and SKPFM experiments were carried out under work function mode, and the areas with higher work function appear brighter. The AFM image of the cast ZG21 sample after exposure to air for 12 h is shown in Fig. 3. The two-dimension (2-D) AFM image (Fig. 3a) and line profile (Fig. 3b) obviously reveal that the $Mg_3Zn_3Gd_2$ second phases protrude from the Mg matrix after mechanical polishing. The height difference between the second phases and the Mg matrix is

approximately 250 ± 100 nm. The same regions, as shown in Fig. 3a, were immersed in 3.5 % NaCl solution for 10 min, and the corrosion morphologies are shown in Fig. 4. Several corrosion pits appear immediately around the second phases (Fig. 4a), whereas the second phases look intact.

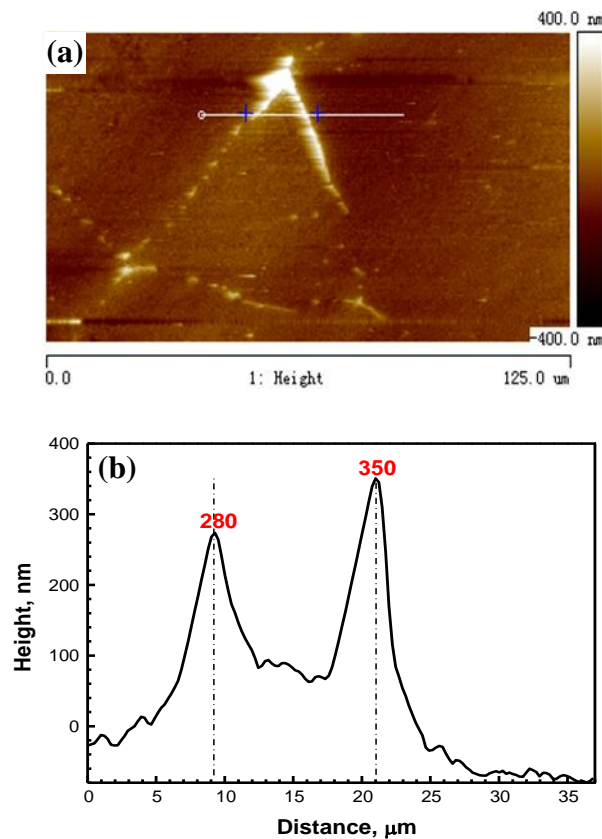


Figure 3. AFM results of the cast ZG21 Mg alloy after exposure to air for 12 h: (a) two-dimension AFM image, and (b) line profile recorded in (a)

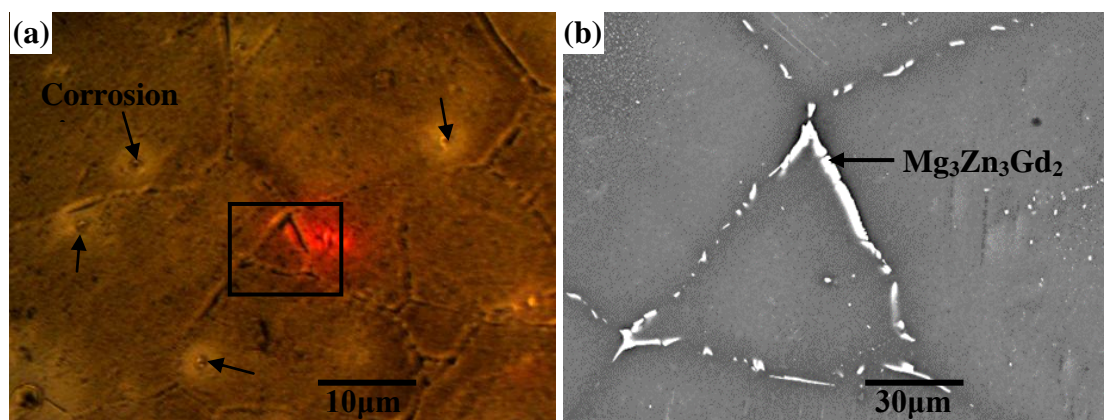


Figure 4. Surface images of the target grain in the cast ZG21 Mg alloy after exposure to 3.5 wt.% NaCl for 10 min: (a) Optical image, and (b) SEM image

The two-dimension (2-D) AFM image of the cast specimen which has been exposed in 3.5 wt.% NaCl solution for 10 min is shown in Fig. 5. The line profile (Fig. 5b) shows that the height difference between the $Mg_3Zn_3Gd_2$ phases and the α -Mg matrix is approximately 320 ± 100 nm. The height differences before and after exposure to NaCl solution vary from 250 ± 100 nm to 320 ± 100 nm. This change can be attributed to the effect of the surface oxide film formed on the second phases and the Mg matrix in NaCl solution.

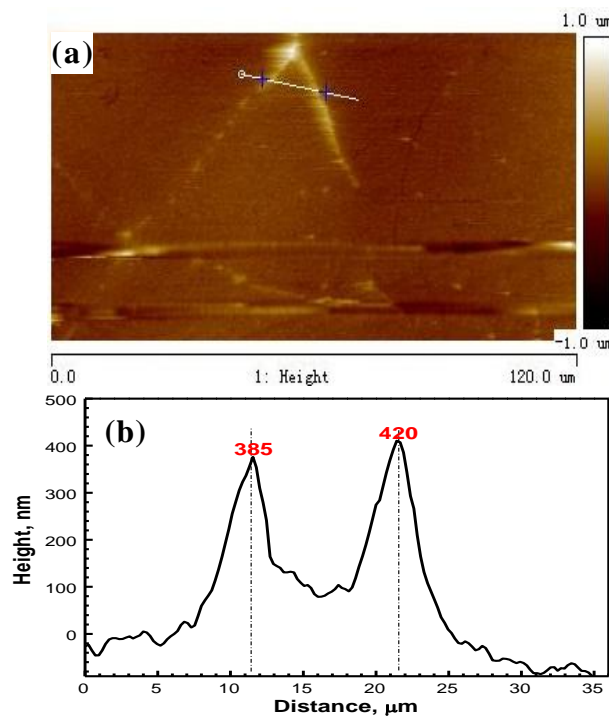


Figure 5. AFM results of the cast ZG21 Mg alloy after exposure to 3.5 wt.% NaCl for 10 min: (a) two-dimension AFM image, and (b) line profile recorded in (a)

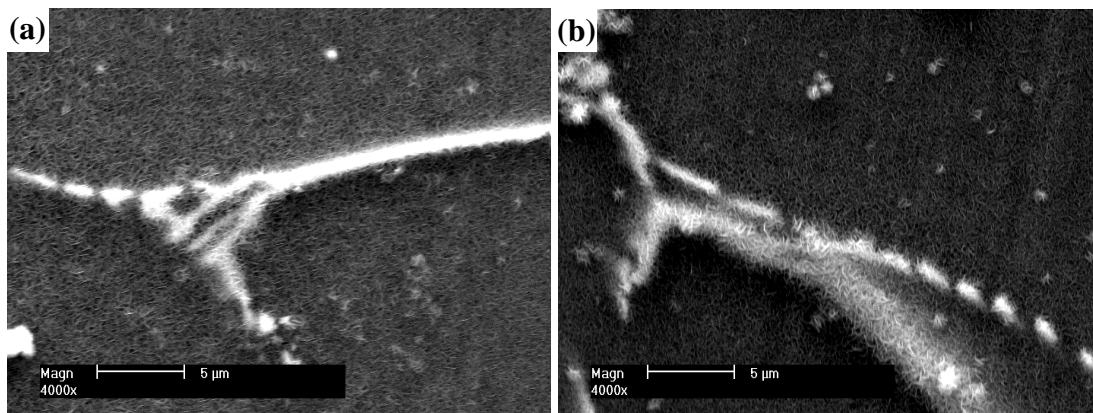


Figure 6. SEM morphologies of the oxide film formed on the cast ZG21 after 1 h (a) and 4 h (b) of immersion in 3.5 wt.% NaCl solution

Fig. 7 shows the Volta potential distribution of the cast ZG21 alloy after exposure to air for 12 h at the same location as SEM and AFM measurements in Fig. 4. The color distribution of the map is

non-uniform (Fig. 7a). The central regions of the α -Mg matrix are darker than the regions near the second phases. In comparison with the target grain (Fig. 4), the brighter areas are the $Mg_3Zn_3Gd_2$ phases. The Volta potential value of the $Mg_3Zn_3Gd_2$ phases is up to 75–86 mV, whereas that of the α -Mg matrix is below zero (Fig. 7b). It is clear that the Volta potential distribution of the cast ZG21 alloy is inhomogeneous. The $Mg_3Zn_3Gd_2$ phases exhibit nobler Volta potential than the α -Mg matrix. It provides a convicitive evidence to prove the possible micro-cathodic role of the $Mg_3Zn_3Gd_2$ phases during the micro-galvanic corrosion process.

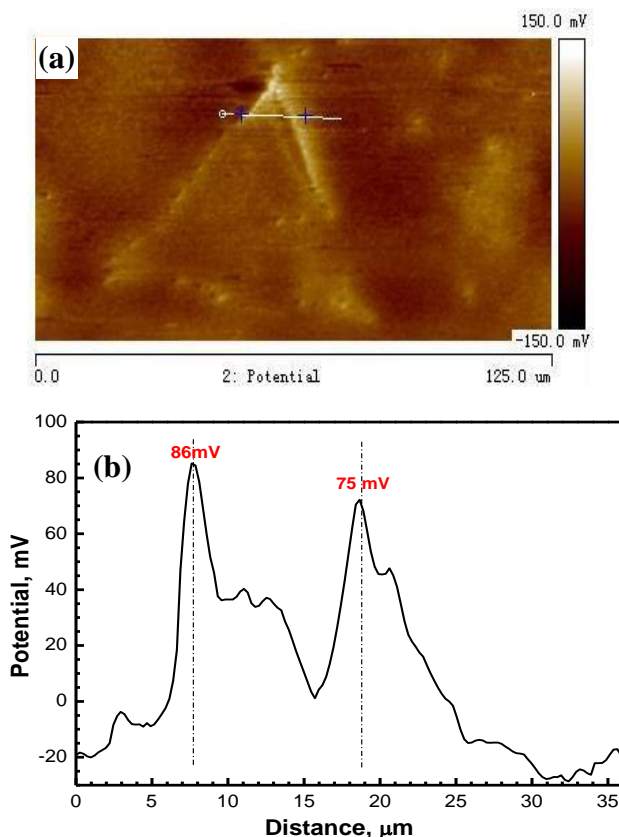


Figure 7. SKPFM results of the cast ZG21 Mg alloy after exposure to air for 12 h: (a) two-dimension SKPFM image, and (b) line profile recorded in (a)

To further clarify the influence of the $Mg_3Zn_3Gd_2$ phases on the corrosion mechanism in detail, several specimens were immersed in 3.5 wt.% NaCl solution for different interval of time (starting from 30 min to 24 h), and then the corrosion morphologies are observed using SEM after the removal of corrosion products. Fig. 8a and b show the corrosion morphologies of the cast samples after 30 min of immersion. The grain boundaries and scattered corrosion pits can be observed clearly from the low magnification view of the morphology (Fig. 8a). Most of these corrosion pits localize in the vicinities of the $Mg_3Zn_3Gd_2$ phases. The circular pits with a scale of nearly 10 μm (Fig. 8b) are the main corrosion forms at this stage. It seems that the second phases do not undergo attack.

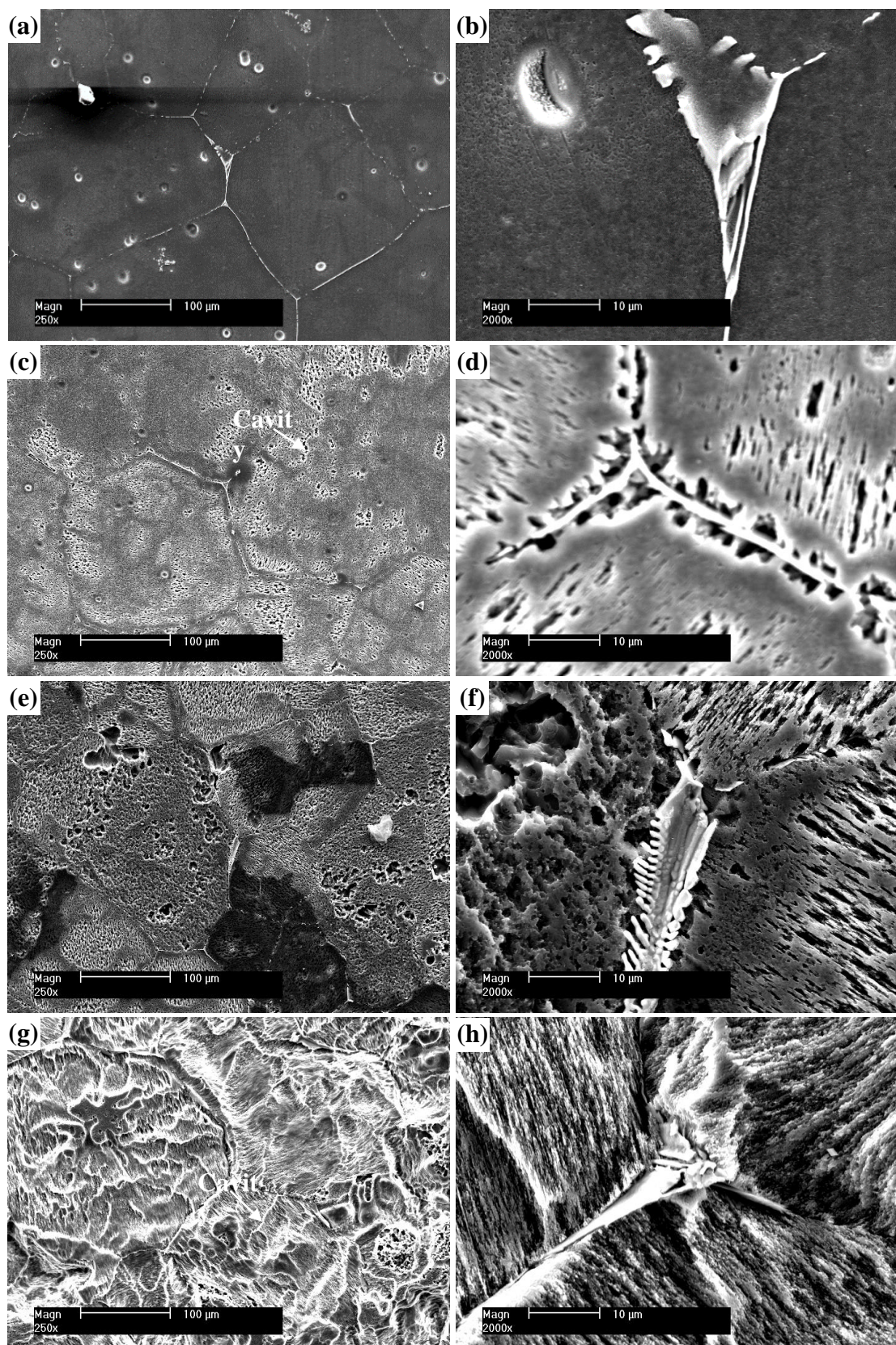


Figure 8. Surface morphologies of the cast ZG21 Mg alloy exposed to 3.5 wt.% NaCl solution for various time with removal of corrosion products: (a, b) 30 min, (c, d) 1 h, (e, f) 5 h, and (g, h) 24 h

The corrosion morphologies of the cast samples after 1 h of immersion are shown in Fig. 8c and d. Abundant small corrosion pits spread over all the Mg matrix, and most of the previous corrosion pits extend to cavities (Fig. 8c). Severe attack of the Mg matrix in the vicinities of the $Mg_3Zn_3Gd_2$ phases along the grain boundaries is observed from the high magnification view of the morphology (Fig. 8d), whereas the $Mg_3Zn_3Gd_2$ phases are still intact. This result clearly demonstrates that the $Mg_3Zn_3Gd_2$ phases act as micro-cathodes during the micro-galvanic corrosion process.

Fig. 8e and f show the corrosion morphologies of the samples after 5 h of immersion. The cavities size further enlarges in comparison with 1 h of immersion (Fig. 8e). Especially, the corrosion near the second phases becomes more severe and there are many deep corrosion pits observed, whereas the second phases do not undergo attack and still keep skeletal structure.

The corrosion morphologies of the cast samples immersed in 3.5 wt.% NaCl for 24 h are shown in Fig. 8g and h. The entire sample suffers severe attack and exhibits a very rough surface (Fig. 8g). The Mg matrix near the second phases has already been corroded out a considerable depth, and the intact $Mg_3Zn_3Gd_2$ second phases evidently protrude from the α -Mg matrix (Fig. 8h).

The above corrosion morphologies clearly indicate that the second phases act as strong micro-cathodes to keep intact whereas the Mg matrix acts as micro-anodes to be corroded. Thus, the size, quantity and distribution of the second phases will greatly affect the corrosion resistance of ZG21 alloy. To clarify this case, the cast and rolled ZG21 are investigated in view of the great difference of second phases in both alloys.

3.3 Macro corrosion morphologies and corrosion rate by immersion tests

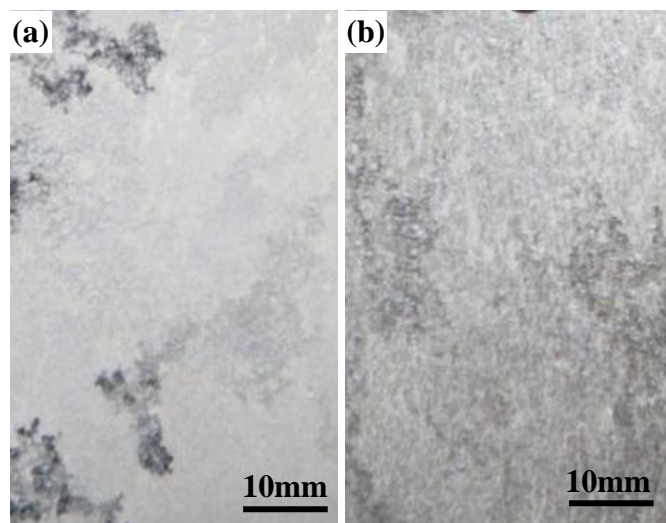


Figure 9. Optical corrosion images of ZG21 Mg alloys after exposure to 3.5 wt.% NaCl for 72 h: (a) cast, and (b) rolled

The macro corrosion morphologies of the cast and rolled alloys after immersion in 3.5 wt.% NaCl solution for 72 h are shown in Fig. 9. Some large and deep corrosion areas appear on the cast ZG21 alloy (Fig. 9a), and most of the other surface suffers slight attack. The corrosion form of the cast

ZG21 alloy is named as localized corrosion. The entire surface of the rolled alloy is corroded slightly, and the corrosion pits are shallow and relatively uniform (Fig. 9b). It is a typical general corrosion form. In comparison with the widespread use of AZ31 sheets suffering severe attack in 0.1 M NaCl for 6 h [37], the rolled ZG21 presents a better corrosion resistance. Combined with the microstructures of the cast and rolled ZG21 alloys, it indicates that the corrosion forms are determined by the size and distribution of the $Mg_3Zn_3Gd_2$ second phases.

Corrosion rate of the cast and rolled samples was compared by immersion tests in 3.5 wt.% NaCl solution for 72 h. Weight loss rates of both alloys are shown in Fig. 10. The cast sample exhibits a higher weight loss rate than the rolled alloy, indicating that the rolled sample is less susceptible to corrosion. However, the rolled alloy exhibits a higher corrosion rate than the traditional Mg alloys of AZ91, AM60 and pure Mg [38, 39].

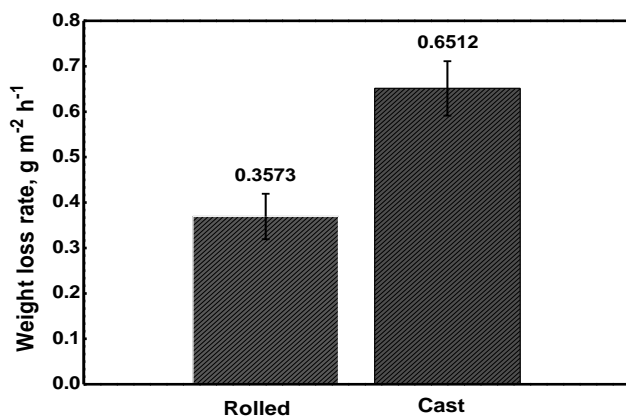


Figure 10. Weight loss rate of the cast and rolled ZG21 Mg alloys after exposure to 3.5 wt.% NaCl solution for 72 h

3.4 Comparison of corrosion resistance by electrochemical measurements

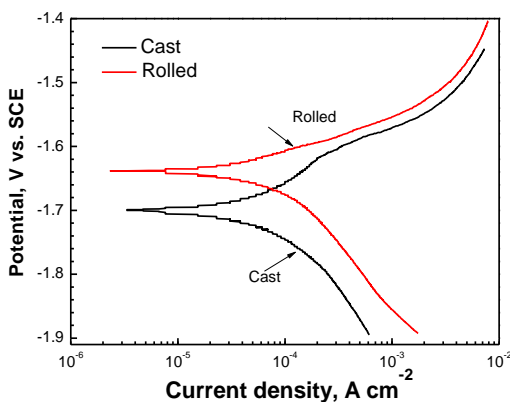


Figure 11. Polarization curves of the cast and rolled ZG21 Mg alloys in 3.5 wt.% NaCl solution

The potentiodynamic polarization curves of the cast and rolled ZG21 Mg alloys in 3.5 wt.% NaCl solution are shown in Fig. 11. Both samples show metallic dissolution reaction instead of passivity at the anodic sides. The rolled alloy exhibits a lower anodic current density, indicating the

slower dissolution rate. The E_{corr} , Tafel slope, and i_{corr} values are listed in Table 1. The rolled alloy shows more positive E_{corr} and lower i_{corr} compared with the cast alloy. This result indicates that the corrosion resistance of the rolled alloy is superior to the cast alloy.

Table 1. Fitting results of the polarization curves

	E_{corr} (V _{SCE})	i_{corr} ($\mu\text{A cm}^{-2}$)	b_a (mV decade $^{-1}$)	$-b_c$ (mV decade $^{-1}$)
Cast ZG21	-1.72	51.3	105.9	100.4
Rolled ZG21	-1.62	20.8	81.3	92.6

The Nyquist spectra (Fig. 12a) of the cast and rolled alloys are characterized by two well-defined capacitance loops at high and medium frequencies followed by an inductance loop in low frequency. The high frequency capacitance loop is attributed to the charge transfer reaction in the electric double layer that localizes at the interface of Mg substrate and corrosive media. The larger diameter of the high frequency capacitance loop means the slower dissolution rate of Mg substrate. The medium frequency capacitance loop is related to film effect. The shape of both plots is similar, but the rolled alloy exhibits markedly larger dimension of Nyquist plot than the cast alloy.

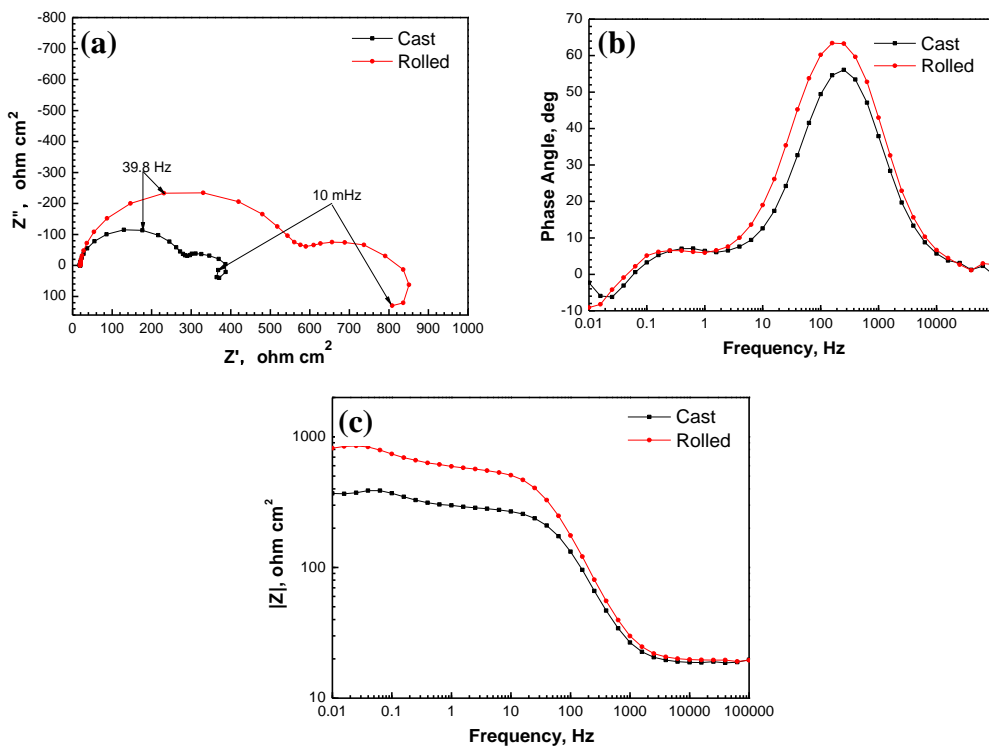


Figure 12. EIS plots of ZG21 Mg alloys in 3.5 wt.% NaCl solution at OCP: (a) Nyquist plots, (b) Bode plots of Degree vs. Frequency, and (c) Bode plots of $|Z|$ vs. Frequency

Bode plots of degree vs. frequency include two wave crests and one wave trough (Fig. 12b), corresponding to the existence of two capacitance loops and one inductance loop in the Nyquist plots.

The Bode plots of $\log |Z|$ vs. frequency (Fig. 12c) show that the impedance values tend to increase with increasing frequency at high and medium frequencies, but the impedance values slightly reduce at low frequency regions. The rolled sample displays a higher impedance value at all of the frequency region. The decrease of impedance values at low frequency corresponds to the existence of inductance loop. The EIS results indicate that the rolled alloy exhibits better corrosion resistance than the cast alloy.

In order to further clarify the corrosion characteristics of both alloys, the impedance data were fitted according to the equivalent circuits in Fig. 13. The fitting results are listed in Table 2.

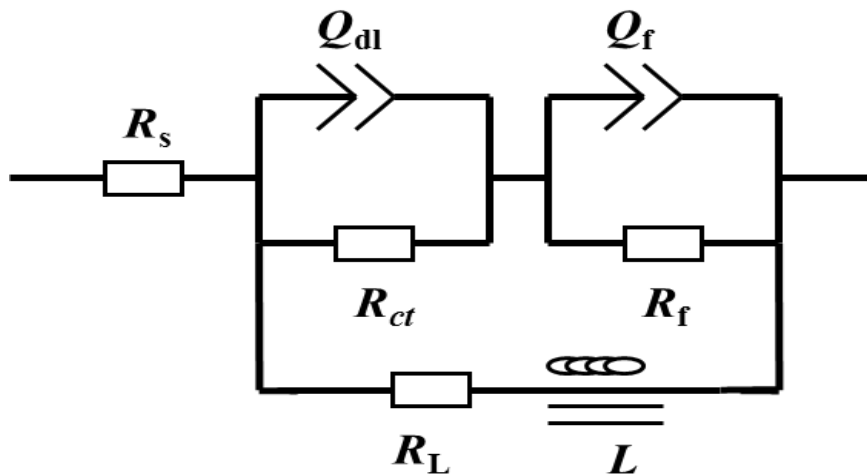


Figure 13. Equivalent circuit of the EIS plots

Table 2. Fitting resulting of the EIS spectra

	R_s ($\Omega \text{ cm}^2$)	Q_{dl} ($\mu\text{S cm}^{-2} \text{ s}^{-n}$)	n_{dl}	R_{ct} ($\Omega \text{ cm}^2$)	Q_f ($\mu\text{S cm}^{-2} \text{ s}^{-n}$)	n_f	R_f ($\Omega \text{ cm}^2$)	R_L ($\Omega \text{ cm}^2$)	L (H cm^2)
Cast ZG21	18.3	6.7	0.69	254.9	171.0	0.93	157.2	883.7	11240
Rolled ZG21	19.2	3.0	0.95	549.9	138.5	0.93	237.6	185.4	2147

R_s is the solution resistance. R_{ct} and Q_{dl} are used to describe the first capacitance loop in high frequency. R_{ct} is the charge transference resistance. Q_{dl} is the double layer capacitance at the interface of electrolyte solution and Mg substrate. Constant phase element Q_{dl} is used in place of a capacitor to compensate the non-homogeneity in the system. Generally, the higher R_{ct} value implies the lower dissolution rate of Mg substrate. R_f and Q_f represent the film resistance and capacity, respectively, which are used to describe the second capacitance loop in medium frequency. The existence of second capacitance loop can be attributed to the corrosion product films on the surface of Mg alloys. L and R_L represent the inductance and inductance resistance, respectively. They are used to describe the low frequency inductance loops. The low frequency inductance loop is due to the initiation of localized corrosion. The fitting results in Table 2 show that the R_{ct} value for the rolled alloy is larger than the cast alloy, implying the lower dissolution rate of the rolled alloy.

4. DISCUSSION

The heterogeneous microstructure of Mg alloys can lead to the electrochemical inhomogeneity. Second phases play the most significant role in the inhomogeneous surface, further to accelerate the micro-galvanic corrosion. The influence of second phases on the corrosion behavior of ZG21 is analyzed as follows.

4.1 Relative nobility of the second phases

SKPFM, AFM and SEM have been applied to investigate the relative nobility of the second phases and Mg matrix in cast ZG21 alloy.

It is known that SKPFM allows direct measurement of the local Volta potential values resulting from complex microstructure. Thus, the electrochemical nobility of the second phases and Mg matrix can be speculated based on the SKPFM relative Volta potential results. The SKPFM results show that the second phases present a positive Volta potential value of approximately 75-86 mV, whereas the α -Mg matrix presents a negative value (Fig. 7b). It is clear that the second phases are nobler than the α -Mg matrix. The Volta potentials measured by the SKPFM are mainly affected by the kinds and contents of the alloy elements. The reason for different Volta potentials on the surface of the cast ZG21 Mg alloys is related to the different contents of Mg, Zn and Gd elements. Combined with the EDS and XRD analysis, the second phases contain more Zn and Gd in comparison with Mg matrix. Literature [40] reported that the second phases which contain more noble elements or the elements which are easy to form oxide layer on the surface have higher Volta potential. Thus, the second phases in case ZG21 show high electrochemical nobility and will serve as microcathodes to accelerate the corrosion of Mg matrix. The AFM and SEM results further prove the microcathodic role of second phases.

The AFM images (Fig. 3 and Fig. 5) indicate that the entire scanned surface is not flat. The $Mg_3Zn_3Gd_2$ second phases protrude from the polished surface, which can be attributed to the higher hardness of the $Mg_3Zn_3Gd_2$ intermetallic compound than the Mg matrix. The height difference between the second phases and the Mg matrix further increases after immersion in NaCl solution for 10 min. It is due to that the $Mg_3Zn_3Gd_2$ second phases act as micro-cathodes and the α -Mg matrix act as micro-anodes during the micro-galvanic corrosion process. The α -Mg matrix around the second phases is dissolved ($Mg \rightarrow Mg^{2+} + 2e^-$), whereas hydrogen evolution reaction occurs on the second phases ($2H_2O + 2e^- \rightarrow 2OH^- + H_2$). The second phases only provide sites for reduction reaction and themselves still keep intact. The local pH around the second phases rises after hydrogen evolution reaction, resulting in the deposition of oxide film on second phases ($Mg^{2+} + 2OH^- \rightarrow Mg(OH)_2$). As a result, the height of the initial second phases further increases after covering with oxide film. For the Mg matrix, on one hand it will sink due to the dissolution reaction. On the other hand, oxide film can also be formed on it. Overall the effect of dissolution reaction and film formation, the height of Mg matrix changes little. In comparison with the increase height of second phases, the height difference is inevitable to increase.

Further, the corrosion morphologies of the cast samples after immersion in 3.5 wt.% NaCl solution for different time intervals (Fig. 8) provide more convictive evidence for the micro-cathodic role of the Mg₃Zn₃Gd₂ phases. The corrosion pits initiate in the vicinities of second phases. The second phases still keep intact after long-term immersion, whereas the surrounding Mg matrix suffers severe attack. These phenomena well prove that the Mg₃Zn₃Gd₂ second phases act as micro-cathodes to accelerate the corrosion of Mg matrix. This result is in good agreement with the more positive Volta potential of second phases by SKPFM measurement.

4.2 Influence of size and distribution of second phases

After the relative nobility of the second phases is clarified, the influence of size and distribution of second phases on the corrosion forms and corrosion resistance is clarified by comparing the cast and rolled ZG21 Mg alloys. There are many previous literatures focusing on the effect of second phases on the corrosion behavior of Mg alloys [41-43]. However, the investigations about the corrosion forms and the quantitative relationship between the corrosion rate and second phases are far away from enough.

The optical corrosion images shows that severe localized corrosion occurs on the cast alloy (Fig. 9a), whereas general corrosion occurs on the rolled alloy (Fig. 9b). The corrosion types, localized corrosion or general corrosion, depend mainly on the size and distribution of the second phases. The large and discrete second phases in the cast ZG21 can extend to the interior of the Mg matrix a considerable depth. The initial small corrosion pits are prone to develop toward depth direction along the second phases due to the micro-cathodic acceleration effect. The second phases in the rolled alloy are fine and is uniformly distributed on the entire surface (Fig. 1b). Micro-galvanic acceleration effect of the fine second phases is weak. Abundant weak micro-galvanic corrosion cells spread all over the surface, resulting in the general corrosion of the rolled sample.

The quantitative relationship between the corrosion rate and second phases can be calculated as follows [44]. The total hydrogen evolution current, including on second phases and α-Mg matrix, is equal to the anodic dissolution current under galvanic potential (E_g) .

$$I_{1,a} = I_{1,c} + I_{2,c} \quad (1)$$

$$i_{1,a}S_1 = i_{1,c}S_1 + i_{2,c}S_2 \quad (2)$$

where $I_{1,a}$ is the anodic dissolution current of α-Mg matrix; $I_{1,c}$ is the hydrogen evolution current of α-Mg matrix; $I_{2,c}$ is the hydrogen evolution current of second phases; $i_{1,a}$ is the anodic dissolution current densities of α-Mg matrix; $i_{1,c}$ is the hydrogen evolution current densities of α-Mg matrix; $i_{2,c}$ is the hydrogen evolution current densities of second phases; S_1 and S_2 are the surface area of α-Mg matrix and second phases, respectively.

Cathodic reaction is controlled by hydrogen evolution, and the limiting current densities can be expressed as:

$$i_L = i_{2,c} \quad (3)$$

Galvanic current densities can be expressed as:

$$i_g = i_{1,a} - i_{1,c} \quad (4)$$

where i_L is the limiting current densities, i_g is the galvanic current densities.

Therefore, the relationship between the surface area of α -Mg matrix (S_1) and second phase (S_2) can be deduced according to the below equations.

$$i_g = i_L S_2 / S_1 \quad (5)$$

The micro-galvanic current densities are in direct proportion to the surface area of the second phases and are in inverse proportion to the surface area of the α -Mg matrix. Because the surface areas of the second phases in the cast alloy are much larger than that in the rolled alloy, the micro-galvanic corrosion of the cast alloy is much severer than the rolled alloy.

5. CONCLUSIONS

(1) The second phases in the cast ZG21 alloy, with the size of several to tens micrometers, exhibit a network but discrete distribution on the grain boundaries. The second phases in the rolled ZG21 alloy are very fine with the size of several hundred nanometers, and exhibit relatively homogeneous distribution on the entire sample surface. The chemical composition of the second phases in the cast and rolled ZG21 is same, namely, $Mg_3Zn_3Gd_2$.

2. The second phases exhibit nobler potential, and act as micro-cathodes to accelerate the corrosion of Mg matrix.

3. Localized corrosion occurs on the cast alloy ZG21, whereas general corrosion occurs on the rolled alloy ZG21. The corrosion resistance of the rolled alloy is superior to the cast alloy, which can be attributed to the different distribution and size of the second phases in both alloys. The micro-galvanic current densities are in direct proportion to the surface areas of the second phases and are in inverse proportion to the surface areas of the α -Mg matrix.

ACKNOWLEDGEMENTS

This work was supported by the National Natural Science Foundation of China (No. 51471174); the National Key Basic Research Program of China (No. 2013CB632205); and the National Key Research and Development Program of China (No. 2016 YFB0301105).

References

1. M. Kulekci, *Int. J. Adv. Manuf. Technol.*, 39 (2008) 851.
2. H. Friedrich and S. Schumann, *J. Mater. Process. Technol.*, 117 (2001) 276.
3. B. Han, D. Gu, Y. Yang, L. Fang, G. Peng and C. Yang, *Int. J. Electrochem. Sci.*, 12 (2016) 374.
4. H. Tang, T. Wu, F. Xu, W. Tao and X. Jian, *Int. J. Electrochem. Sci.*, 12 (2016) 1377.
5. G. Song, A. Atrens and M. Dargusch, *Corros. Sci.*, 41 (1998) 249.
6. G. Song, A. Atrens, X. Wu and B. Zhang, *Corros. Sci.*, 40 (1998) 1769.
7. R. Ambat, N. Aung and W. Zhou, *Corros. Sci.*, 42 (2000) 1433.
8. N. Dinodi, A. Shetty, *J. Magnes. Alloys*, 1 (2013) 201.
9. A. Atrens, G. Song, F. Cao, Z. Shi and P. Bowen, *J. Magnes. Alloys*, 1 (2013) 177.
10. G. Song and K. Unocic, *Corros. Sci.*, 98 (2015) 758.

11. Y. Song, E. Han, D. Shan, C. Yim and B. You, *Corros. Sci.*, 60 (2012) 238.
12. M. Jönsson, D. Thierry and N. LeBozec, *Corros. Sci.*, 48 (2006) 1193.
13. H. Krawiec, S. Stanek, V. Vignal, J. Lelito and J. Suchy, *Corros. Sci.*, 53 (2011) 3108.
14. Y. Song, D. Shan, R. Chen and E. Han, *Corros. Sci.*, 52 (2010) 1830.
15. Y. Choi, K. Kuroda and M. Okido, *Corros. Sci.*, 103 (2016) 181.
16. G. Song, A. Bowles and D. John, *Mater. Sci. Eng. A*, 366 (2004) 74.
17. O. Lunder, J. Lein, T. Aune and K. Nisancioglu, *Corros. Sci.*, 45 (1989) 741.
18. H. Yang, C. Liu, P. Wan, L. Tan and K. Yang, *APL Materi.*, 1 (2013) 052104-1.
19. J. Liu, Y. Song, J. Chen, P. Chen, D. Shan and E. Han, *Electrochim. Acta*, 189 (2016) 190.
20. J. Liu, Y. Song, D. Shan and E. Han, *J. Electrochem. Soc.*, 163 (2016) C856.
21. Y. Song, D. Shan, R. Chen and E. Han, *Corros. Sci.*, 51 (2009) 1087.
22. T. Zhang, Y. Li and F. Wang, *Corros. Sci.*, 48 (2006) 1249.
23. J. Chen, J. Wang, E. Han and W. Ke, *Corros. Sci.*, 50 (2008) 1449.
24. Z. Yang, J. Li, J. Zhang, G. Lorimer and J. Robson, *Acta Metall. Sin.*, 21 (2008) 313.
25. Q. Jiang, K. Zhang, X. Li, Y. Li, M. Ma, G. Shi and J. Yuan, *J. Magnes. Alloys*, 1 (2013) 230.
26. D. Wu, R. Chen, W. Tang and E. Han, *Mater. Des.*, 41 (2012) 306.
27. H. Yan, R. Chen and E. Han, *Mater. Sci. Eng. A*, 527 (2010) 3317.
28. H. Yan, S. Xu, R. Chen, S. Kamado, T. Honma and E. Han, *Scripta Mater.*, 64 (2011) 141.
29. H. Yan, R. Chen and E. Han, *Mater. Charact.*, 62 (2011) 321.
30. Q. Li, Q. Wang, Y. Wang, X. Zeng and W. Ding, *J. Alloys Compd.*, 427 (2007) 115.
31. R. Arrabal, E. Matykina, A. Pardo, M. Merino, K. Paucar, M. Mohedano and P. Casajús, *Corros. Sci.*, 55 (2012) 351.
32. W. Liu, F. Cao, L. Chang, Z. Zhang and J. Zhang, *Corros. Sci.*, 51 (2009) 1334.
33. S. Zhu, Z. Liu, R. Qu, L. Wang, Q. Li and S. Guan, *J. Magnes. Alloys*, 1 (2013) 249.
34. D. Eliezer, P. Uzan, E. Aghion, *Mater. Sci. Forum*, 419-422 (2003) 857.
35. R. Arrabal, B. Mingo, A. Pardo, E. Matykina, M. Mohedano, M. Merino, A. Rivas and A. Maroto, *Corros. Sci.*, 97 (2015) 38.
36. J. Chen and W. Tsai, *Electrochim. Acta*, 56 (2011) 1746.
37. J. Chen, Y. Song, D. Shan, E. Han, *Corros. Sci.*, 53 (2011) 3281.
38. Y. Choi, K. Kuroda, M. Okido, *Corros. Sci.*, 103 (2016) 181.
39. N. Birbilis, G. Williams, K. Gusieva, A. Samaniego, M. Gibson, H. McMurray, *Electrochim. Commun.*, 34 (2013) 295.
40. S. Wang, J. Ding, H. Ming, Z. Zhang, J. Wang, *Mater. Charact.*, 100 (2015) 50.
41. S. Li, A. Bacco, N. Birbilis, H. Cong, *Corros. Sci.*, 112(2016) 596.
42. M. Zhao, M. Liu, G. Song, A. Atrens, *Corros. Sci.*, 50 (2008) 1939.
43. Y. Song, D. Shan, E. Han, *J. Mater. Sci. Technol.*, <http://dx.doi.org/10.1016/j.jmst.2017.01.014>
44. C. Cao, Corrosion Electrochemistry Principle, Chemical Industry Press, Beijing, 2004 (in Chinese).